Supplement of

Insights into stress-loading mechanisms in the western Peloponnese, Greece from a high-resolution earthquake catalog

David Essing[1], Gian Maria Bocchini[1], Marco Pascal Roth[1], Anna Serpetsidaki[2], Ioanna Nikolopoulou[2], Rebecca Maria Harrington[1], Efthimios Sokos[2]

[1]Institute of Geosciences, Ruhr-University Bochum, Bochum, 44780, Germany
[2] Seismological Laboratory, Geology Department. University of Patras, GR-26504 Patras, Greece

Correspondence to: David Essing (david.essing@rub.de)

Contents of this file

Introduction

This supplemental information provides two text elements describing seismic moment estimation and the complete set of earthquakes detected using the methods described in the main text. The main text considers the set of earthquakes with depths shallower that 1 km from the plate interface. It also contains two tables that document the velocity model used in the NLLoc approach and the quality-control criteria implemented in the moment tensor inversion. It further provides supporting information with 11 additional plots. All supplemental information is referenced in the main text.

Text 1: Seismic moment estimation

We estimate seismic moment to calculate the moment magnitude M_w for the catalog built in this study. We limit the calculation to S-waves because of the higher signal-to-noise ratio (SNR) relative to P-waves.

First, we estimate the time window length for the seismic phase and noise signals. To include the relevant source information for each event, we choose magnitude-dependent time windows of sufficient length to contain the frequency with peak energy content, assuming a conservative estimate of low stress drop, while avoiding contamination from secondary phases. We first calculate an upper and lower time-window limit by the inverse of a theoretical corner frequency corresponding to stress drop values of 10 MPa and 0.01 MPa, respectively. Second, we follow the approach from Bindi et al. (2020) to estimate an optimal time window length for source parameter estimation, which is based on phase energy of individual stations measured from the integral of the squared velocity (Izutani & Kanamori, 2001). Our time window starts 0.7 seconds before the

designated phase pick and ends at 90% (for hypocentral station-event distance < 25 km), 80% (distance 25 - 50 km), or 70% (distance > 50 km) of the cumulative energy for a dynamic stationwise estimate. If the energy-based time window is larger or shorter than the upper bounds estimated by stress drop, we use the longer time window.

Next, we remove the instrument response from the raw data, convert to velocity, and apply a filter in a frequency band specialized for each event and station. Filter frequency limits are based on the expected peak energy for the magnitude. For the lower corner, we start with a conservative frequency range that covers 80% to 100% of a theoretical stress drop of 0.005 MPa. If the conservative estimate is at frequencies beyond which the instrument response is flat, we use the lower corner of the instrument response. If the conservative estimate is higher than 3 Hz, we use a lower corner of 3 Hz. The upper corner estimate is either 40 to 45 Hz, or 90 to 95 Hz, and is dictated by the Nyquist frequency.

We estimate S-wave and noise spectra from the vector sum of all three components at each station using a multi-taper spectral estimation (Prieto, 2022). We convert instrument-response-removed velocity spectra to displacement by integrating in the frequency domain to avoid spectral contamination that may arise from non-periodic components of the static displacement (Madariaga et al., 2019, Schliwa and Gabriel, 2024). We exclude stations with SNR < 3, where we evaluate the SNR from the lower filter corner of the instrument response removal up to the frequency where spectral amplitude drops by 20 dB relative to the flat part of the spectrum, but not higher than 30 Hz.

We resample displacement spectra to log-linear intervals in the frequency band of SNR > 3 and subsequently fit them according to a Boatwright source model (Boatwright, 1980),

$$\Omega(f) = \Omega_0 \frac{e^{-\frac{\pi f t}{Q}}}{\left(1 + \left(\frac{f}{f_c}\right)^{\gamma n}\right)^{\frac{1}{\gamma}}}, \quad (1)$$

where t is the source-station travel time. We allow the long-period spectral amplitude Ω_0 to vary between 80% and 120% of the maximum observed amplitude during fitting to compensate for artifacts. The shape controlling factor γ is set to 2, the high frequency falloff rate n, and the seismic attenuation Q, are set to constant values of Q = 600 and n = 2.125. We allow the fitted spectral corner frequency f_c to vary in the range of resampled frequencies. We note that estimates of other source parameters, such as static stress drop require a more detailed consideration of the selection of Q, n, and allowed ranges for f_c, since they undergo an inherent trade-off during fitting. As the long period spectral amplitude is the most stable value during fitting, and the others are not key to the magnitude estimation, we do not consider them in greater detail here. Finally, we estimate seismic moment, M_0, using the long period spectral amplitude, Ω_0, using (Eqn 1; Brune, 1970).

$$M_0 = \frac{4\pi\rho\beta^3\Omega_0 R}{U_{\phi\Theta}}. \quad (2)$$

In the equations above, R is the hypocentral distance, and $U_{\Phi\Theta}$ is the radiation pattern, with an assumed value of 0.63 for S-waves (Aki & Richards, 2002). The depth-dependent shear wave velocity β comes from Kassaras et al. (2014) and Sachpazi et al. (2020) and has a gradient between layers. Values range from 2486 to 4530 km s^{-1} from the surface down to 105 km depth. We estimate the rock formation density ρ using the Nafe-Drake curve (Ludwig et al., 1970), hand-picked from Brocher, (2005). The density ranges from 2.46 to 3.36 g cm^{-3}. We calculate M_w with

$$M_w = \frac{\log_{10}(M_0)}{1.5} - 6.07, \quad (3)$$

(Kanamori and Brodsky, 2004). In cases of multiple station estimates per event, we report the mean value.

Text 2: Description of the Earthquake Catalog for the entire Region

Picks for all events in the catalog total 245,078, leading to the detection and location of 21,331 earthquakes, following the association of picked phase arrivals (Fig. 2). Fig. 2a summarizes the complete catalog resulting from the workflow described in Section 2. It shows the contribution of stations whose numbers of picks for located events ranges from 487 to 20,542. The stations in the centre of the Peloponnese generally contribute the highest number of picks, while those near the shoreline contribute comparatively fewer.

Applying SSSTs and coherence-based location methods to the entire catalog reduces the average length of the horizontal semi-minor- and semi-major-axis of the 68% confidence ellipsoid from 1.62 and 3.84 km to 0.83 and 1.32 km, which corresponds to a decrease of ~50 %. The average vertical error decreases by the same order of magnitude from 2.75 to 1.49 km. As noted in the main text, the description of the catalog is restricted to the upper plate seismicity, which is the focus of this study. The subset of upper-plate events with well-resolved locations have horizontal semi-major axis errors of < 5 km, vertical errors < 5 km, and an RMS < 0.5. The average length of the horizontal semi-minor- and semi-major-axis of the 68% location confidence ellipsoid are 0.85 and 2.24 km length; the average vertical error is 1.52 km and the average RMS is 0.17 s (Fig. S5). The estimated M_L values range from –0.3 to 5.8 with an M_c = 1.1 and *b*-value = 1.1 ± 0.02 (Fig. S6b). We were able to retrieve Mw from spectral estimates for 3,076 events in a range from M_w 0.2 to 5.8. We use a linear regression with resulting *R*-value of 0.98 to determine the M_w - M_L scaling relationship $M_w = 0.83 \cdot M_L + 0.62$ (Fig. S6c).

Table 1: Combined 1-D velocity layers of Kassaras et al. (2014) with the lower layers of Sachpazi et al. (2020) used for NNLoc event location and MT solutions.

Depth (km)	Vp (km/s)	Vp gradient (km/s/km)
-2	4.3	0.1
0	4.5	0.15

4	5.1	0.136
10	5.92	0.068
15	6.26	0.005
21	6.29	0.091
28	6.93	0.048
35	7.27	0.085
43	7.95	0.006
51	8	0.004
75	8.1	0.003
105	8.2	0

Table 2: Moment Tensor (MT) solutions of the 5 largest events in the upper-plate crust analyzed here. "Centroid depth" is determined by the MT inversion; str, dip, rak are strike, dip, rake respectively; dc is the percentage double couple component; Mw is moment magnitude, Mo is seismic moment; nst is the number of stations used in the inversion; VR is the variance reduction; CN is the condition number; FMVR is the Focal Mechanism variability Index; STVR is Space-Time variability Index.

date	**Clat**	**Clon**	**cdepth**	**str**	**dip**	**rak**	**dc**	**Mw**	**Mo**	**nst**	**VR**	**CN**	**FMVR**	**STVR**
240513_1356	37.532	21.6729	1.5	325	35	-101	83	3.8	5.59E+14	10	65	3.2	11	0.037
240706_1734	37.8327	21.1839	10.5	18	89	-166	68	4.8	1.94E+16	11	82	1.9	4.2	0.224
240707_1441	37.844	21.1945	10.5	209	66	13	90	4.5	6.42E+	12	76	1.6	7.6	0.209

	9					1			15					
240714_0739	37.8345	21.1812	12.5	26	81	-159	75.6	3.5	1.89E+14	11	71	2.2	4.8	0.167
240922_1827	37.8204	21.83	8.5	272	49	-126	77.1	4	1.12E+15	8	83	2.1	7	0.221

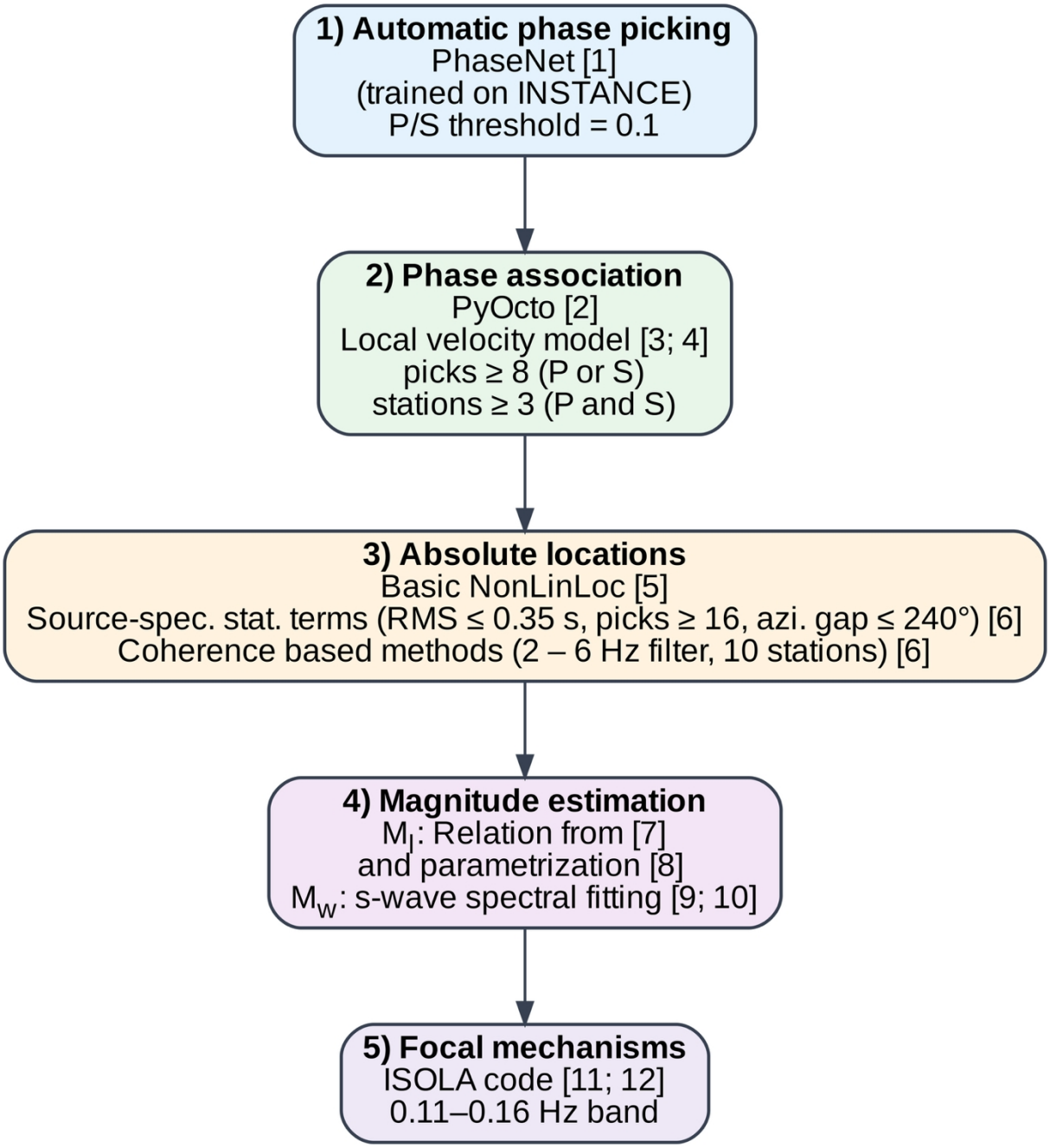

Figure S1: Catalog-building workflow that consists of 1) phase picking using PhaseNet (Zhu & Beroza, 2019) trained with the INSTANCE dataset (Michelini et al, 2021); 2) event association using PyOcto (Münchmeyer, 2023) with a combined velocity model (Kassaras et al., 2014; Sachpazi et al., 2020); 3) High-resolution absolute location estimation using NLLoc (Lomax et al., 2000; Lomax & Savvaidis, 2022); 4) local magnitude (M_L) estimation following Hutton & Boore (1987) using parameters from Scordilis et al. (2016), and Moment magnitude (M_w) estimation by spectral fitting with a Boatwright (1980) model 5) Focal mechanisms estimation using ISOLA (Sokos & Zahradnik, 2008; Zahradnik & Sokos, 2018). [1] Zhu & Beroza, 2019 [2] Münchmeyer, 2023 [3] Kassaras et al., 2014 [4] Sachpazi et al., 2020 [5] Lomax et al., 2000 [6] Lomax & Savvaidis, 2022 [7] Hutton & Boore, 1987 [8]

Scordilis et al., 2016 [9] Boatwright, 1980 [10] Kanamori & Brodsky, 2004 [11] Sokos & Zahradnik, 2008 [12] Zahradnik & Sokos, 2018

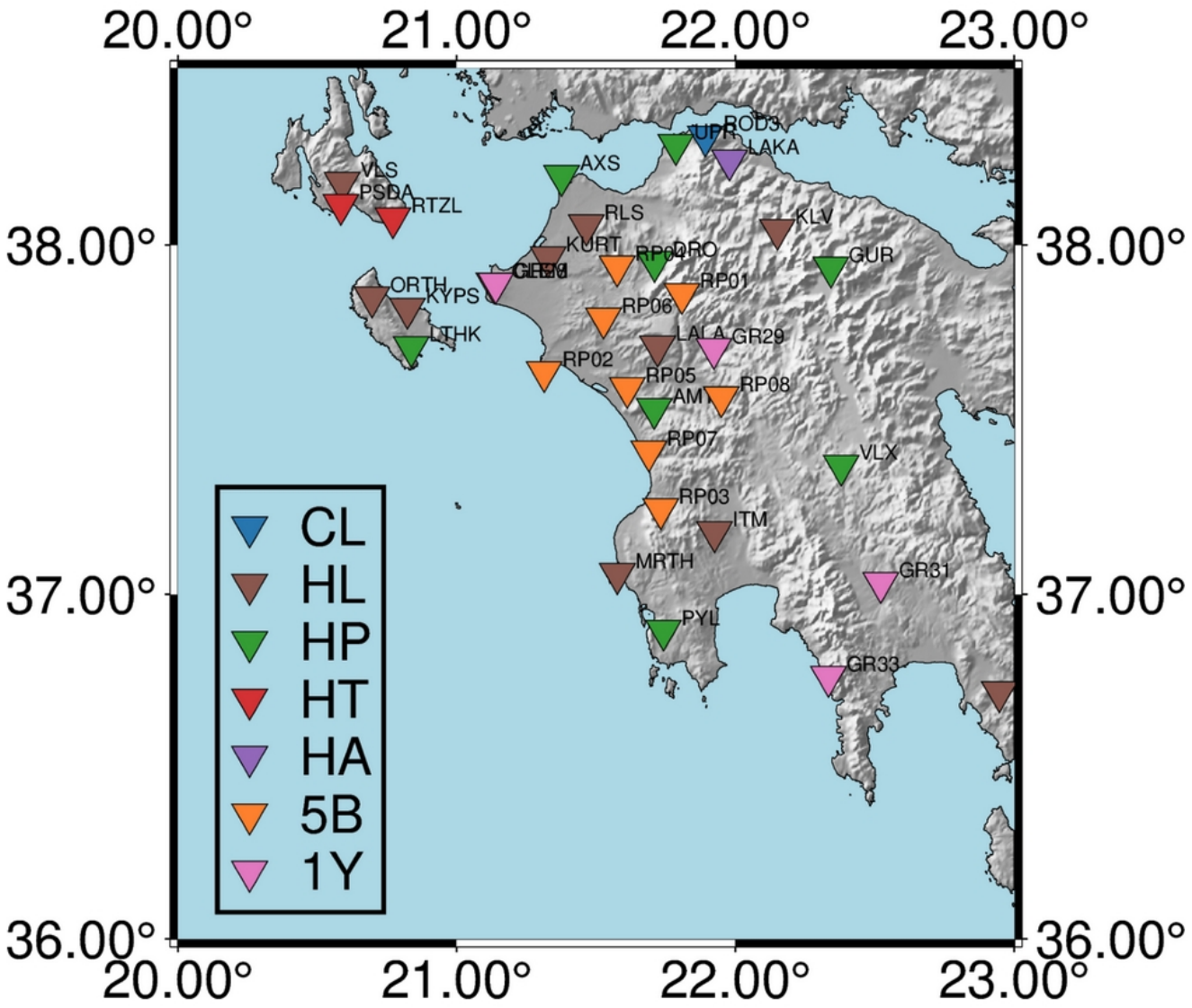

Figure S2: Combined (temporary (1Y, 5B) and long-term) station network used for this work with station names.

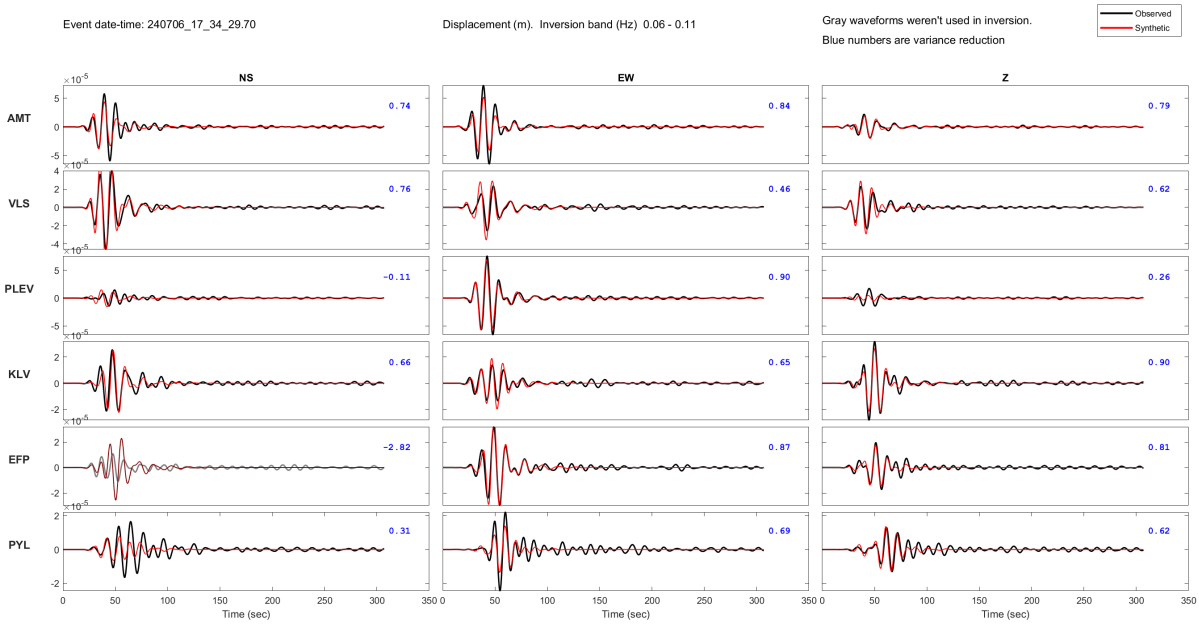

Figure S3: Observed and synthetic waveforms from the moment tensor (MT) inversion for a representative event (M4.8 on 06 July 2024) observed near Vartholomio and modeled at 6 stations.

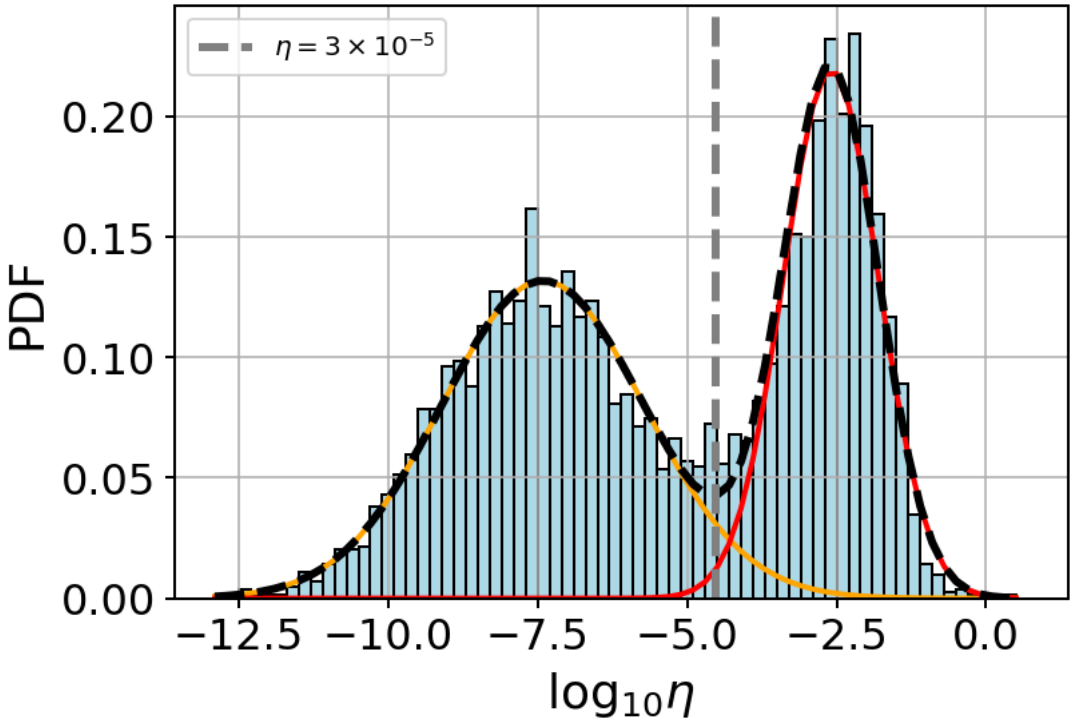

Figure S4: Distribution of the nearest neighbor distances η according to the Gaussian-Mixture model. The vertical dashed line indicates the cluster threshold separating background (e.g., Poissonian) and clustered (e.g., non-Poissonian) seismicity.

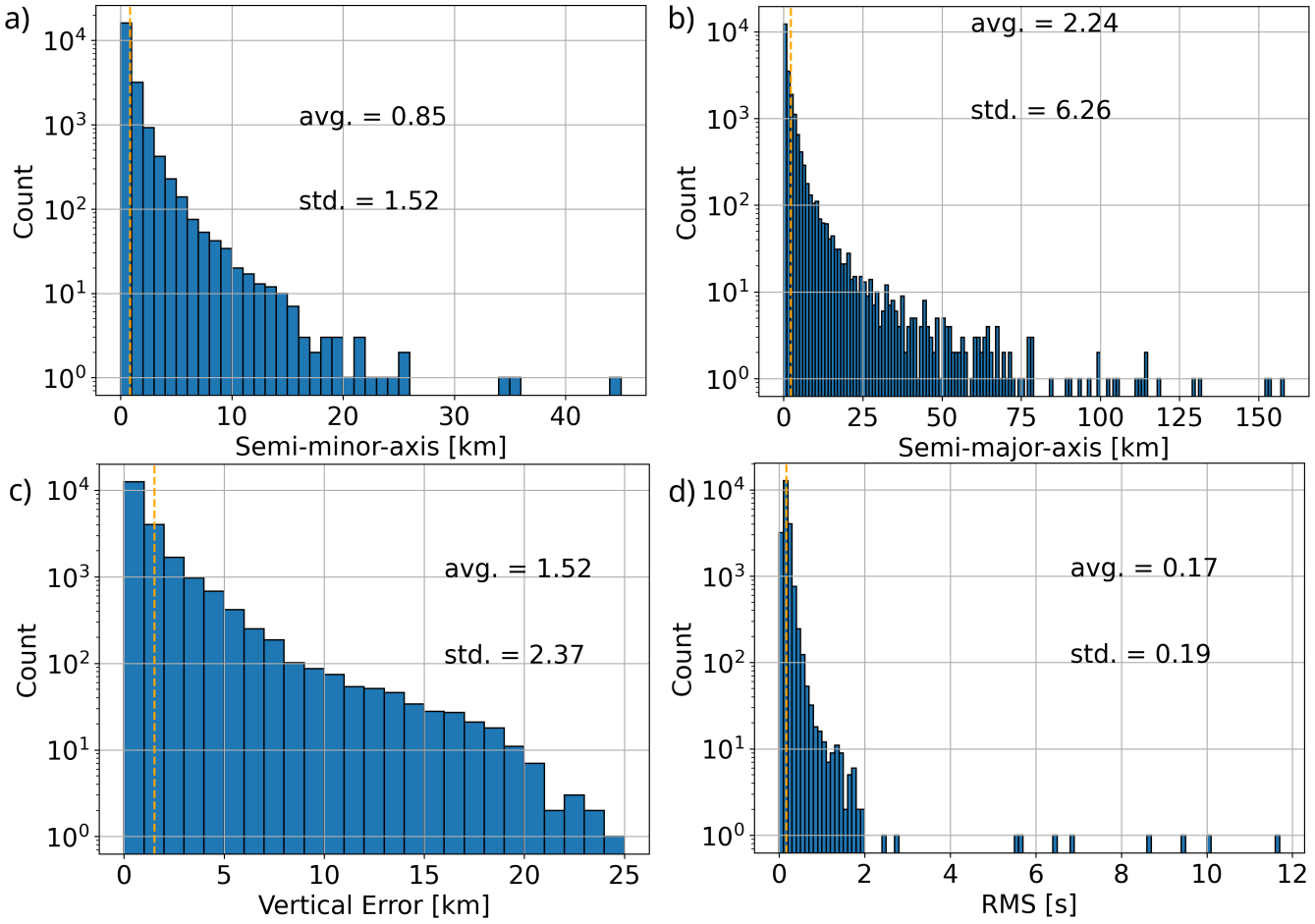

Figure S5: Precision estimation of the locations for the entire catalog (a) Distribution of the length of the horizontal semi-minor-axis of the 68% confidence ellipsoid. (b) as (a) but for the horizontal semi-major-axis. (c) as (a) but for the vertical errors. (d) as (a) but for the root-mean-square (RMS) values.

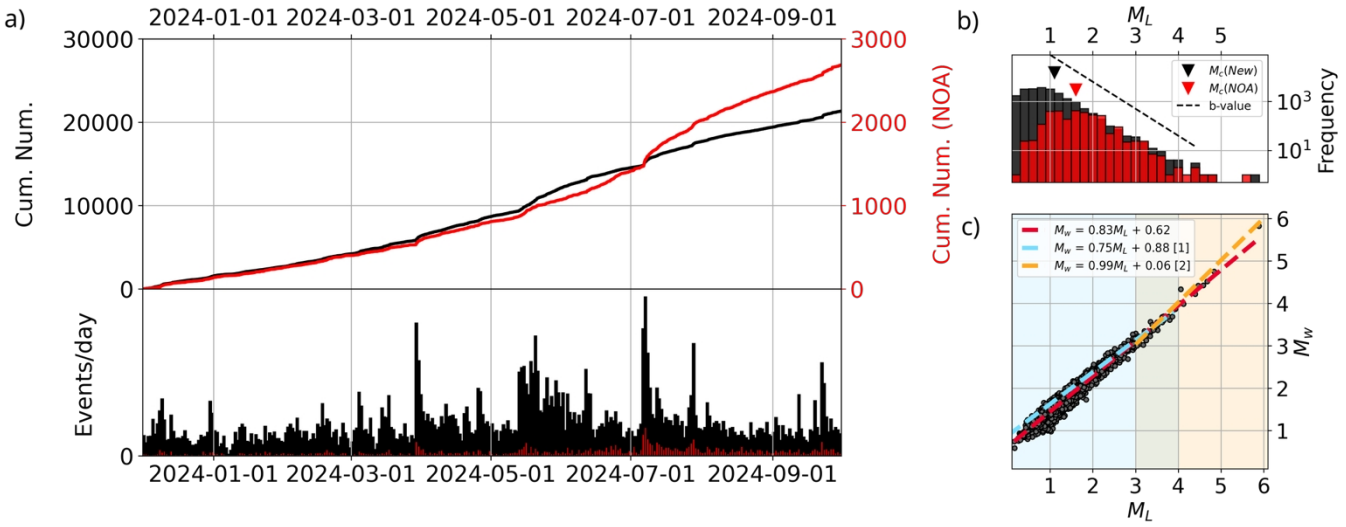

Figure S6: (a) Cumulative number of the detected seismicity (black) relative to the cumulative number of seismicity listed in the catalog of the National Observatory of Athens (NOA) indicated in red. Note the two different y-axes. Event rate in 2-day time windows. (b) Frequency-Magnitude distribution for the local Magnitude (M_L) distribution of the NOA catalog and the full catalog built here. The magnitude of completeness (M_c) = 1.1 for the new catalog as well as for the NOA catalog (M_c=1.6) is indicated, estimated with a Maximum Curvature method adding a constant offset of 0.2 to obtain the final value (Wiemer & Wyss 2000; Woessner & Wiemer 2005). The b-value for the new catalog of 1.1 is indicated, estimated following van der Elst (2021). (c) Estimated moment magnitudes (M_w) as a function of M_L. Red dashed line indicates the fit to the crustal seismicity of this data-set, blue dashed line and shaded area are the fit and magnitude range found in [1] Ross et al. (2016), and orange dashed line and shaded areas are the fit and magnitude range used in [2] Konstantinou et al. (2018).

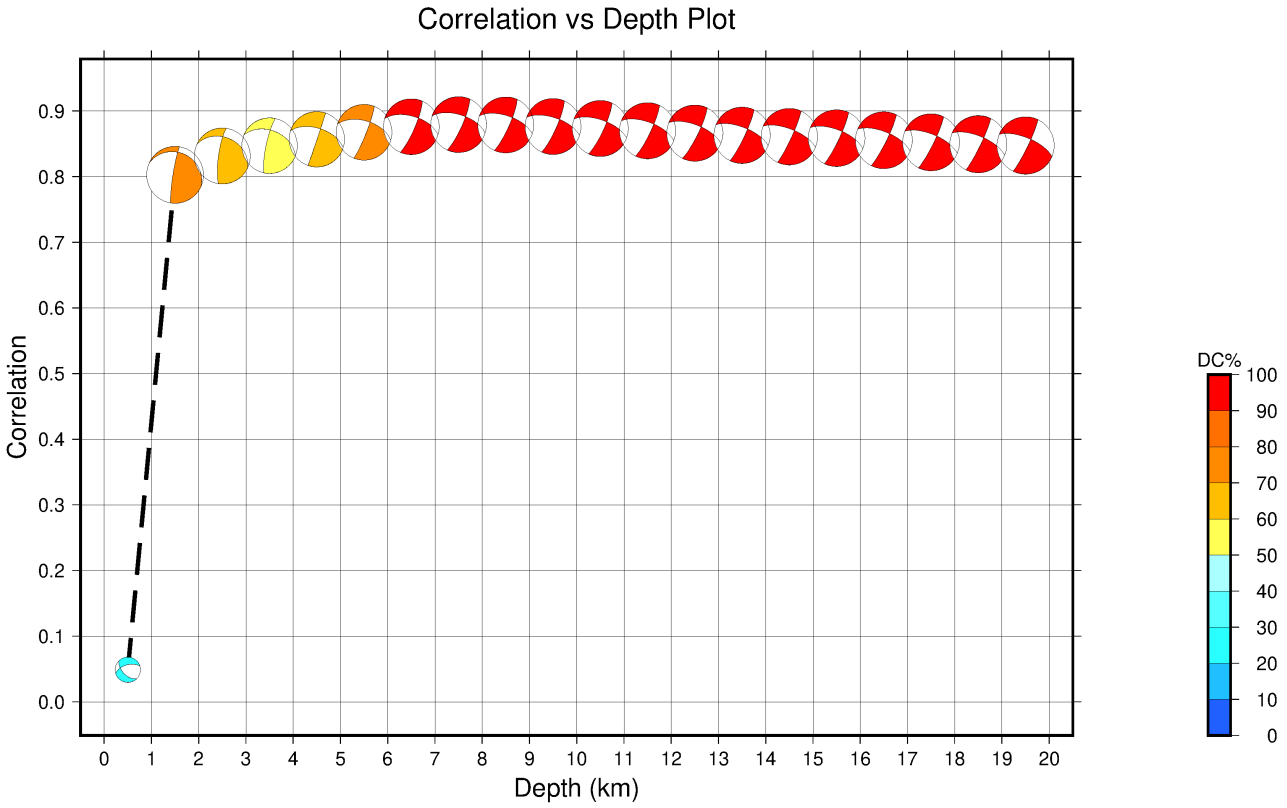

Figure S7: Solution stability as a function of depth for the moment tensor inversion of the example event of Fig. S3.

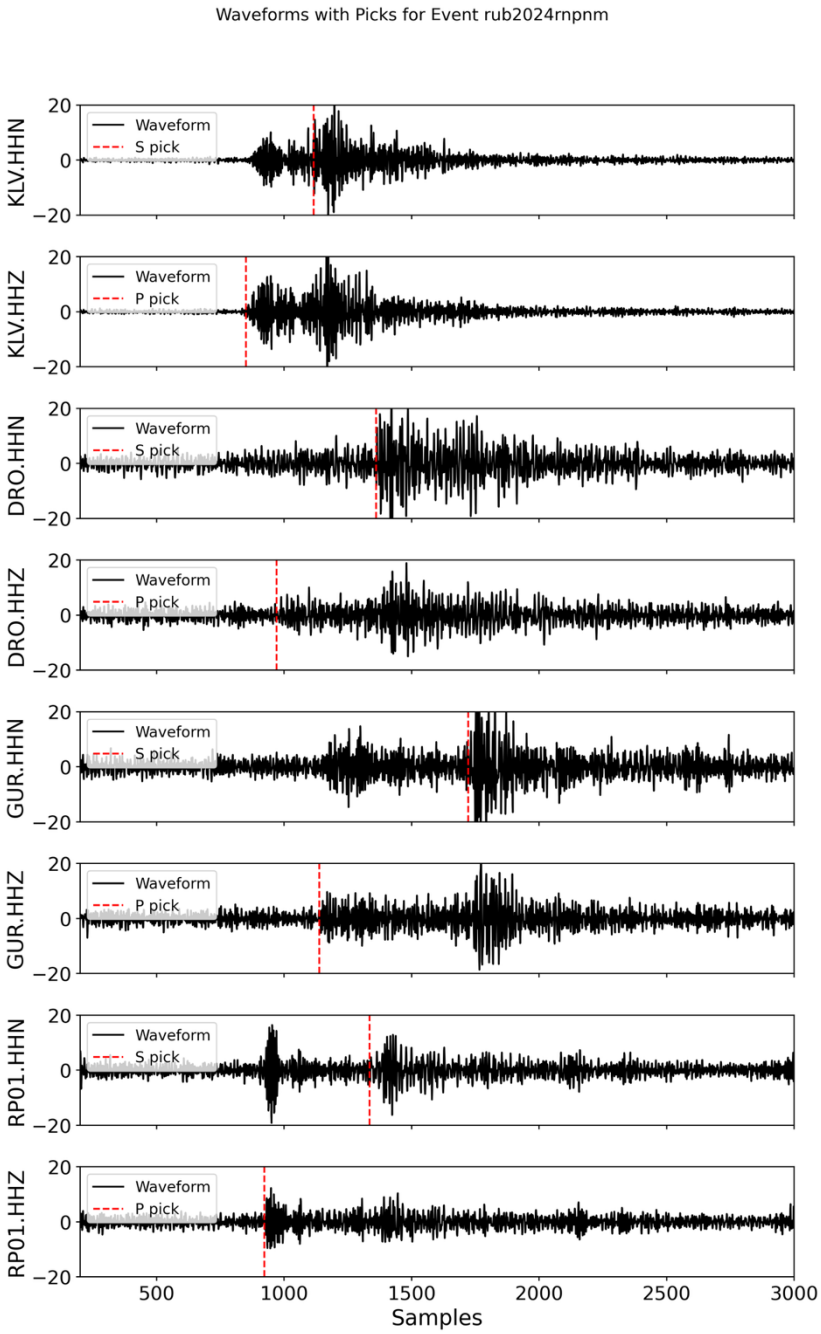

Figure S8: Waveforms (5B.RP01 downsampled to 100 Hz) and related picks from stations that detected the smallest magnitude earthquake in the catalog presented in this work (M_L = -0.2).

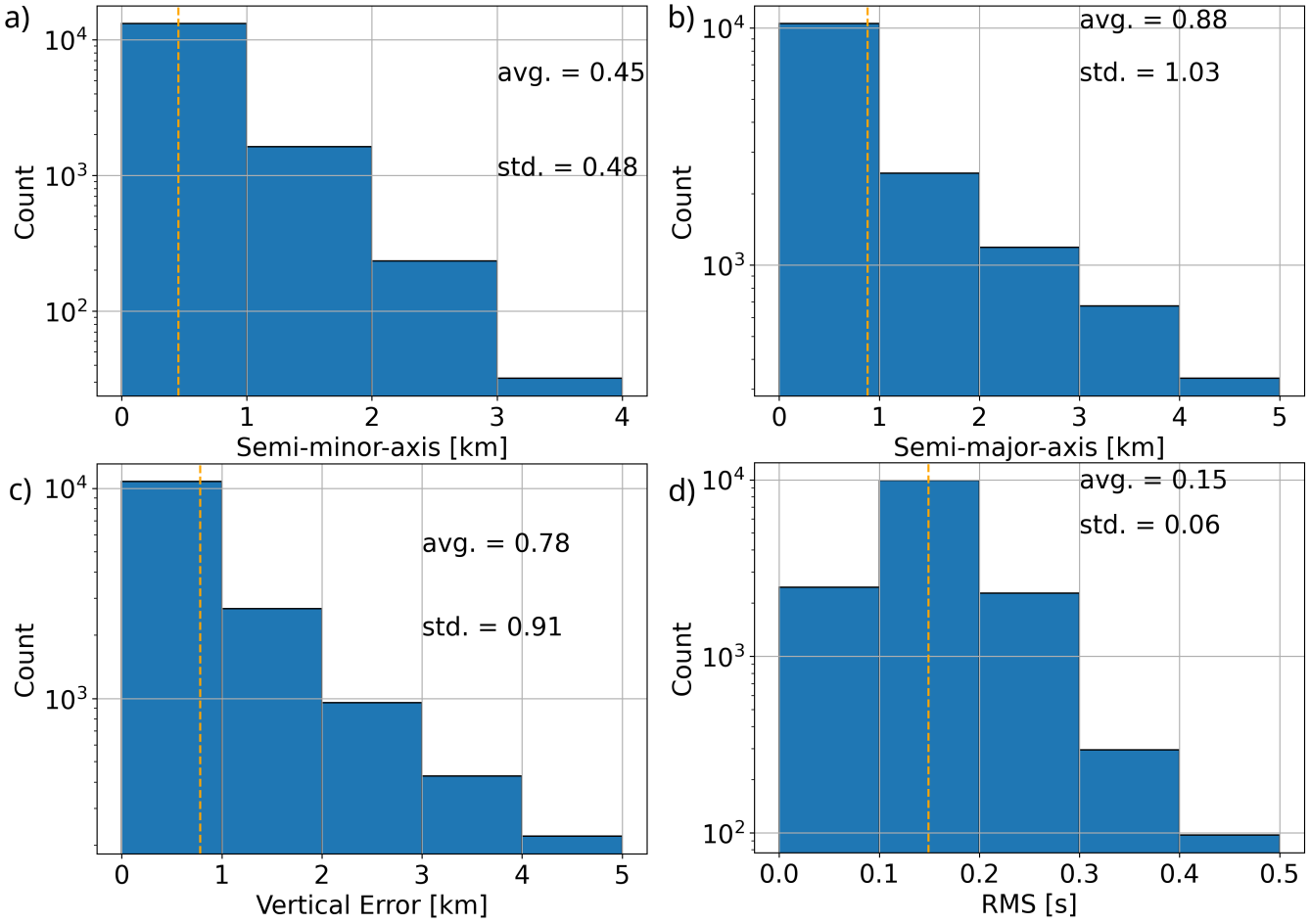

Figure S9: As Fig. S6, but for the crustal seismicity (1 km above the slab model of Bocchini et al., 2018), with an RMS < 0.5 s, a semi-major-axis of the 68% confidence ellipsoid < 5 km, and a vertical error < 5 km.

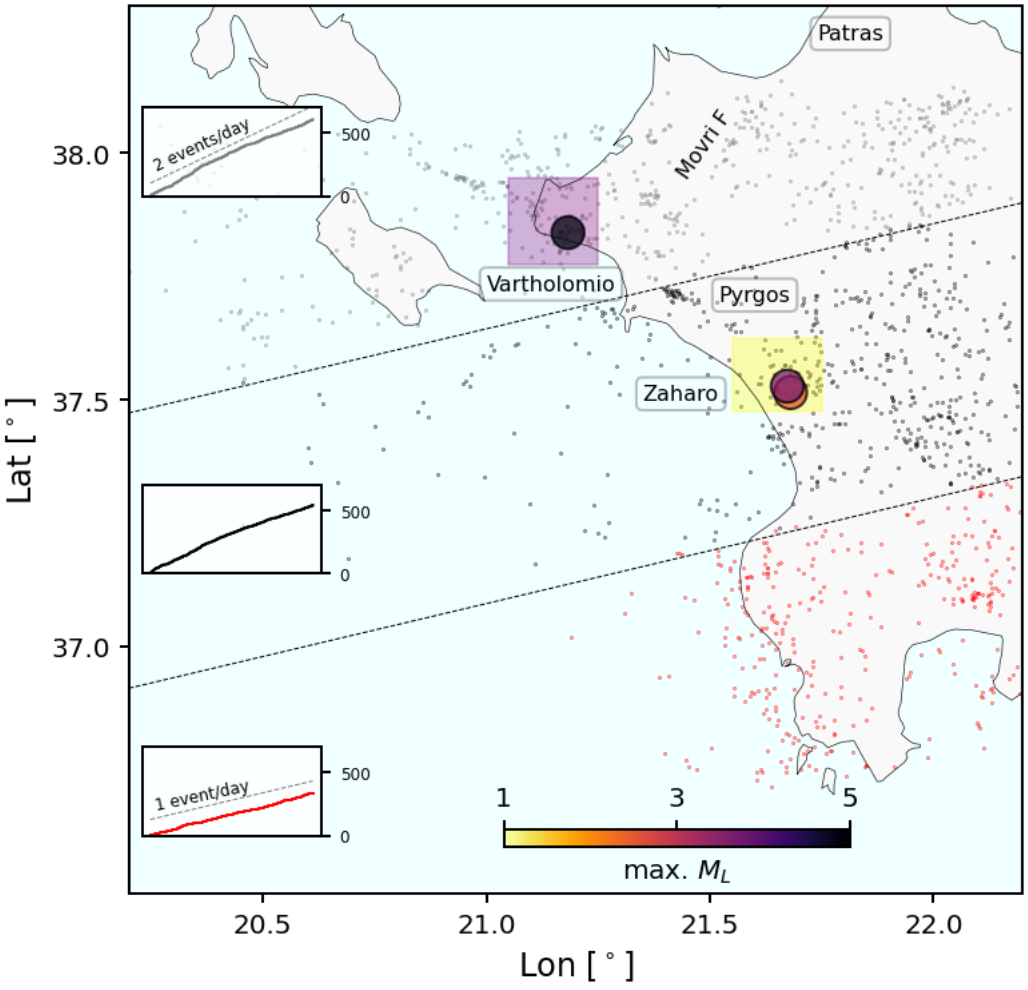

Figure S10: Map of the study area. Small dots (grey, black, red) indicate background seismicity as seen in Fig. 4b, subdivided into three subregions along strike of the subducting slab (as opposed to along latitutde, as presented in the text). Large dots indicate cluster centroid locations of the three largest earthquake clusters (N > 100) as seen in Fig. 4c. Clusters are color-coded by their largest local magnitude (M_L). A region of elevated background seismicity is seen west to the city of Pyrgos. Insets: Cumulative number of background earthquakes for each subregion. For the northern and southern subregion, a reference event rate is indicated.

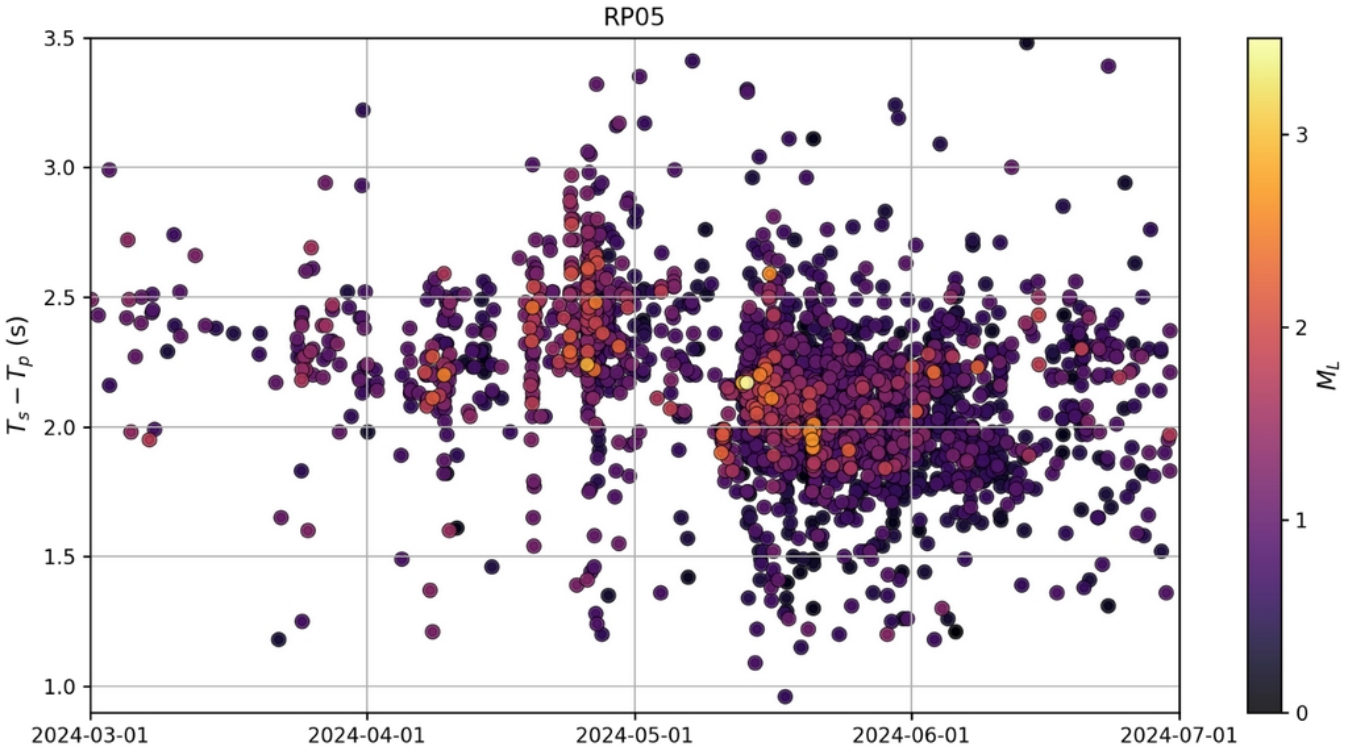

Figure S11: Ts-Tp times in seconds as picked during the Zaharo sequence at RP05. From 2024-03-01, a decrease of the Ts-Tp, indicates migration of seismicity towards station RP05 (Fig. S2). The observed decrease in Ts-Tp times is followed by an increase in April 2024 that translates to a migration of the seismicity away from RP05. A general decrease of the Ts-Tp times in May 2024 indicate another migration episode toward RP05.

Data Set S1 (Earthquake Catalog)

Bocchini et al. (2025)

References

Aki, K., & Richards, P. (2002). Quantitative seismology. MIT Press.

Bindi, D., Spallarossa, D., Picozzi, M., & Morasca, P. (2020). Reliability of source parameters for small events in central Italy: Insights from spectral decomposition analysis applied to both synthetic and real data. Bulletin of the Seismological Society of America, 110(6), 3139-3157.

Boatwright, J. (1980). A spectral theory for circular seismic sources; simple estimates of source dimension, dynamic stress drop, and radiated seismic energy. Bulletin of the Seismological Society of America, 70(1), 1-27.

Bocchini, G. M., Essing, D., & Roth, M. (2025). High-resolution earthquake catalog and focal mechanism solutions for the western Hellenic subduction system (Greece) [Data set]. Zenodo. https://doi.org/10.5281/zenodo.17641018

Bocchini, G. M., Brüstle, A., Becker, D., Meier, T., Van Keken, P. E., Ruscic, M., ... & Friederich, W. (2018). Tearing, segmentation, and backstepping of subduction in the Aegean: New insights from seismicity. *Tectonophysics*, *734*, 96-118.

Brocher, T. M. (2005). Empirical relations between elastic wavespeeds and density in the Earth's crust. Bulletin of the seismological Society of America, 95(6), 2081-2092.

Brune, J. N. (1970). Tectonic stress and the spectra of seismic shear waves from earthquakes. Journal of geophysical research, 75(26), 4997-5009.

Hutton, L. K., & Boore, D. M. (1987). The ML scale in southern California. Bulletin of the Seismological Society of America, 77(6), 2074-2094.

Izutani, Y., & Kanamori, H. (2001). Scale-dependence of seismic energy-to-moment ratio for strike-slip earthquakes in Japan. Geophysical research letters, 28(20), 4007-4010.

Kanamori, H., & Brodsky, E. E. (2004). The physics of earthquakes. Reports on progress in physics, 67(8), 1429.

Kassaras, I., Kapetanidis, V., Karakonstantis, A., Kouskouna, V., Ganas, A., Chouliaras, G., ... & Makropoulos, K. (2014). Constraints on the dynamics and spatio-temporal evolution of the 2011 Oichalia seismic swarm (SW Peloponnesus, Greece). Tectonophysics, 614, 100-127.

Konstantinou, K. I., & Melis, N. S. (2018). The relationship between local and moment magnitude in Greece during the period 2008–2016. Pure and Applied Geophysics, 175, 731-740.

Lomax, A., & Savvaidis, A. (2022). High-precision earthquake location using source-specific station terms and inter-event waveform similarity. Journal of Geophysical Research: Solid Earth, 127(1), e2021JB023190.

Lomax, A., Virieux, J., Volant, P., & Berge-Thierry, C. (2000). Probabilistic earthquake location in 3D and layered models: Introduction of a Metropolis-Gibbs method and comparison with linear locations. In Advances in seismic event location (pp. 101-134). Dordrecht: Springer Netherlands.

Ludwig, W. J., Nafe, J. E., & Drake, C. L. (1970). Seismic refraction. The Sea: ideas and observations on progress in the study of the seas, (1).

Madariaga, R., Ruiz, S., Rivera, E., Leyton, F., & Baez, J. C. (2019). Near-field spectra of large earthquakes. Pure and Applied Geophysics, 176(3), 983-1001.

Michelini, A., Cianetti, S., Gaviano, S., Giunchi, C., Jozinović, D., & Lauciani, V. (2021). INSTANCE–the Italian seismic dataset for machine learning. Earth System Science Data, 13(12), 5509-5544.

Münchmeyer, J. (2023). PyOcto: A high-throughput seismic phase associator. arXiv preprint arXiv:2310.11157.

Prieto, G. A. (2022). The multitaper spectrum analysis package in Python. Seismological Society of America, 93(3), 1922-1929.

Ross, Z. E., Ben-Zion, Y., White, M. C., & Vernon, F. L. (2016). Analysis of earthquake body wave spectra for potency and magnitude values: Implications for magnitude scaling relations. Geophysical Supplements to the Monthly Notices of the Royal Astronomical Society, 207(2), 1158-1164.

Sachpazi, M., Kapetanidis, V., Charalampakis, M., Laigle, M., Kissling, E., Fokaefs, A., ... & Hirn, A. (2020). Methoni Mw 6.8 rupture and aftershocks distribution from a dense array of OBS and land seismometers, offshore SW Hellenic subduction. Tectonophysics, 796, 228643.

Schliwa, N., Gabriel, A. A., & Ben-Zion, Y. (2025). Shallow fault zone structure affects rupture dynamics and ground motions of the 2019 Ridgecrest sequence to regional distances. Journal of Geophysical Research: Solid Earth, 130(6), e2025JB031194.

Scordilis, E. M., Kementzetzidou, D., & Papazachos, B. C. (2016). Local magnitude calibration of the Hellenic unified seismic network. Journal of Seismology, 20, 319-332.

Sokos, E. N., & Zahradnik, J. (2008). ISOLA a Fortran code and a Matlab GUI to perform multiple-point source inversion of seismic data. Computers & Geosciences, 34(8), 967-977.

van der Elst, N. J. (2021). B-positive: A robust estimator of aftershock magnitude distribution in transiently incomplete catalogs. Journal of Geophysical Research: Solid Earth, 126(2), e2020JB021027.

Wiemer, S., & Wyss, M. (2000). Minimum magnitude of completeness in earthquake catalogs: Examples from Alaska, the western United States, and Japan. Bulletin of the seismological society of America, 90(4), 859-869.

Woessner, J., & Wiemer, S. (2005). Assessing the quality of earthquake catalogues: Estimating the magnitude of completeness and its uncertainty. Bulletin of the Seismological Society of America, 95(2), 684-698.

Zahradník, J., & Sokos, E. (2018). ISOLA code for multiple-point source modeling. In Moment tensor solutions: A useful tool for seismotectonics (pp. 1-28). Cham: Springer International Publishing.

Zhu, Weiqiang, and Gregory C. Beroza. "PhaseNet: a deep-neural-network-based seismic arrival-time picking method." Geophysical Journal International 216.1 (2019): 261-273.